International Journal of Nanomaterials and Nanostructures
Vol. 1: Issue 2
www.journalspub.com

Action Potential Monitoring Using Neuronanorobots: Neuroelectric Nanosensors

Nuno R. B. Martins[1*], Wolfram Erlhagen[1], Robert A. Freitas Jr[2].

1 - Center for Mathematics (CMAT), University of Minho, Campos de Azurém, Guimarães, 4800-058, Portugal.

2 - Institute for Molecular Manufacturing, 555 Bryant Street, Suite 354, Palo Alto, California 94301, USA

Abstract

Neuronanorobotics, a key future medical technology that can enable the preservation of human brain information, requires appropriate nanosensors. Action potentials encode the most resource-intensive functional brain data. This paper presents a theoretical design for electrical nanosensors intended for use in neuronanorobots to provide non-destructive, in vivo, continuous, real-time, single-spike monitoring of action potentials initiated and processed within the ~86 x 10^9 neurons of the human brain as intermediated through the ~2.4 x 10^{14} human brain synapses. The proposed ~3375 nm^3 FET-based neuroelectric nanosensors could detect action potentials with a temporal resolution of at least 0.1 ms, enough for waveform characterisation even at the highest human neuron firing rates of 800 Hz.

Keywords: *human brain information, nanorobot, nanorobotics, neuronanorobot, neuronanorobotics, nanomedicine, nanosensor, nanotechnology, synaptobot, endoneurobot.*

***Author for Correspondence:** Email ID: n-martins@n-martins.com*

Abbreviations: *AIS - axon initial segment, BOINC - barcoding of individual neuronal connections, CNT - carbon nanotube, DNA - deoxyribonucleic acid, DWCNT - double-wall carbon nanotube, FET - field-effect transistor, MRI - magnetic resonance imaging, RESCOP - redundant-skeleton consensus procedure, SNR - signal-to-noise ratio, SWCNT - single-wall carbon nanotube, vsNP - voltage sensing inorganic nanoparticle.*

1. INTRODUCTION

Information pertaining to brain neural connectivity (e.g., the connectome) and the associated electrical action potential activity at the cellular and subcellular level, together with other sources of brain structural and functional information, underlies higher mental states and individuality. This information can be lost as a result of physical trauma, pathogenic diseases, and a variety of degenerative disorders. Current medical technology for brain information scanning, either destructive or non-destructive in nature, cannot monitor the structural and functional information of a whole human brain in real-time, *in vivo*, with adequate temporal and spatial resolution.

Technology capable of providing whole human brain, non-destructive, *in vivo*, real-time, functional information with adequate temporal and spatial resolution will have several specific requirements. Such technology would have to monitor, among other brain data, all action potential based functional data traffic passing through (86.06 ± 8.2) x 10^9 human brain neurons[1] and (2.42 ± 0.29) x 10^{14} human brain synapses[2], accurately recording synaptically-processed (4.31 ± 0.86) x 10^{15} spikes/sec[2]. Accomplishing this objective will require appropriate sensing, communication and hardware infrastructure to handle an estimated neuroelectric data rate of (5.52 ± 1.13) x 10^{16} bits/sec for the entire living human brain[2]. This data rate appears necessary to capture even the fastest firing rates in the

400-800 Hz range from fast spiking neurons[4, 5] and eventually to characterise even the fastest voltage velocities at 20 mV/ms[6]. Another requirement is the ability to transmit this huge data flow into an external supercomputer, possibly using an *in vivo* fiber network[7] capable of handling 10^{18} bits/sec of data traffic[7, 2]. Such a fiber network may occupy 30 cm^3 and generate 4-6 W of waste heat[7]. Ideally the transit time from signal origination inside the human brain to the external computer system through such a network would have negligible signal latency in comparison to the action potential waveform temporal resolution[7].

Medical nanorobotics offers an ideal technology for monitoring, recording, and even manipulating many of the different types of brain-related information, in particular functional action potential based electrical information[8, 7, 9, 10, 11, 12, 13, 14, 15, 16, 17, 18]. Medical nanorobotics has received preliminary technical exploration[7, 9, 19, 20] and there are several detailed theoretical designs for a variety of medical nanorobots[8, 21, 22, 23, 24, 25, 20, 27].

Neuronanorobots, a specific class of medical nanorobots, are expected to permit *in vivo*, whole-brain, real-time monitoring of single-neuron neuroelectric activity and local neuropeptide traffic, permitting also the acquisition of all relevant structural information including neuron surface features and connectome mapping [28, 29, 30, 31, 32]. Non-destructive whole-brain monitoring would be enabled by the coordinated activities of large numbers of cooperating neuronanorobots. Medical neuronanorobotics might be the ultimate technology needed to treat Parkinson's and Alzheimer's diseases, other brain-related neurodegenerative disorders, epilepsy, dementia, memory and sensory disorders, spinal cord and neuromuscular disorders, pain and toxic disorders, and a wide variety of traumatic injuries to the brain. Non-medical applications of this promising technology include the possibility of becoming the virtually perfect brain-machine interface technology necessary to finally bridge human brain and machine[33].

The advent of medical neuronanorobotics requires the ability to build nanorobotic devices and to produce these devices in sufficient therapeutic quantities to treat individual patients. The most advanced neuronanorobots will likely be fabricated using diamondoid materials, because these materials provide the greatest strength, durability, and reliability in the *in vivo* environment and have good biocompatibility[9, 20]. Possible methods to achieve massively parallel molecular manufacturing technologies, such as a nanofactory, have been reviewed in the literature[38, 20, 39], and methods for controlling individual and large numbers of medical nanorobots are also the subject of current research[34, 35, 36]. An ongoing international collaboration is pursuing the objective of constructing a nanofactory capable of mass-manufacture medical diamondoid nanorobotic devices for medical treatments[37, 20, 39].

Neuronanorobotic sensors are a key technology for all subclasses of neuronanorobots, especially for endoneurobots (neuron-resident robots) and synaptobots (synapse-monitoring robots). Appropriate monitoring of the different types of functional human brain information requires nanosensors with crucial performance characteristics, including: appropriate dynamic range to capture the entire signal amplitude, high-

accuracy as an appropriate percentage of full scale output, high-sensitivity, small hysteresis permitting good discrimination between similar inputs, low output noise compared with the fluctuation in the physical signal, good resolution for measuring the minimum detectable signal fluctuation with good margins of safety, and appropriate bandwidth with fast response time to a rapid change in physical signal.

After a brief survey of contemporary brain scanning techniques (Section 2) and specific action potential measurement requirements (Section 3), we review appropriate sensor choices (Section 4) and then provide a preliminary design for a specific nanorobot sensor (Section 5) that is intended for use in endoneurobots and synaptobots performing real-time monitoring of *in vivo* action potentials. Nanosensor biocompatibility is briefly addressed in Section 6.

2. CONTEMPORARY BRAIN SCANNING

2.1 Non-Destructive Techniques

Non-destructive structural whole brain monitoring techniques in the form of computerized scanning-based imaging modalities, such as positron emission tomography and magnetic resonance imaging, provide non-destructive three-dimensional views of the brain down to ~1 mm resolution, with typical clinical MRI scan voxel resolutions of 1 mm x 1 mm x 3 mm [40, 41]. Such resolution permits regional analyses of brain structure but is clearly insufficient for investigation of structures underlying intercellular communication at the level of individual neurons or synapses[42]. High-definition fiber tractography provides accurate reconstruction of white matter fiber tracts[43, 44] but also with a resolution of only ~1 mm [43, 44].

Micro-CT scanners, with a typical scan time between 10 min and 2 hr, allow high-resolution tomography of specimens up to a few centimeters in diameter, with the highest spatial resolution being 2 μm, still not enough to detect most synapses. The state-of-the-art tomographic Nano-CT scanners (the Micro-CT successor) achieves structural resolutions between 50-500 nm. Three Nano-CT scanners are commercially available today: the Nanotom, the SkyScan-2011, and the Xradia nanoXCT. The Nanotom provides a resolution of ~500 nm pixels, and handles maximum object size of 150 mm height and 120 mm diameter [45] (roughly the size of a whole human brain). The SkyScan-2011 has a slightly better resolution of ~400 nm pixels with similar object size constraints. The Xradia nanoXCT claims to be capable of providing a spatial resolution between 50-300 nm[46]. Nano-CT scanner resolutions might permit extraction of some cellular detail and eventually identification of some synapses, but much structural information remains uncaptured and, most problematically, the technology does not permit *in vivo* brain scanning.

Current techniques for non-destructive functional whole brain monitoring do enable the creation of detailed system level maps of the brain functional connectome, achieved using resting-state functional magnetic resonance imaging[47] with voxel size resolution of 2 mm x 2 mm x 2.5 mm[48], but these are still incapable of cellular-level resolution.

2.2 Destructive Techniques

Contemporary destructive structural whole brain monitoring can provide resolutions down to the nanometric level. Ultramicrotome scanning, for example, provides near nanometric resolution after chemical preservation of the tissue. It is being used to scan larger and larger brain volumes with nanometric detail permitting visualisation of individual synapses and its components. Ultramicrotome sections 30-100 nm thick are scanned by either a transmission electron microscope, a serial block-face scanning electron microscopy, or a light-optical microscope, with automation of the collection of ultrathin serial sections for large volume transmission electron microscope reconstructions[49, 50, 51]. Current scanned volumes are far from a whole human brain volume, but a process to achieve a whole human brain is envisioned[51]. Several methods were developed to improve the analysis of the ultra-thin microtome images. After scanning, posterior software reconstruction uses specialised software such as RESCOP or KNOSSOS to trace the connections between neurons[52]. Tagging individual neurons with fluorescent proteins[53, 54] facilitates the analysis of neuronal circuitry and glial territory mapping on a large scale. A high-throughput technique called BOINC ("barcoding of individual neuronal connections") for establishing circuit connectivity at single-neuron and synaptic resolution was proposed using high-throughput DNA sequencing[55].

Other strategies are also being pursued to avoid the laborious ultrastructural electron microscopy based techniques. For example, The X-ray nanotomography microscope delivers a high-resolution 3-D image of the entire cell in one step, an advantage over electron microscopy in which a 3-D image is assembled out of many thin sections which can take up to weeks for just one cell[56, 57]. Cell ultrastructure has been imaged with X-rays down to 30 nm resolution.

Partially destructive techniques have been used to study, physiologically and anatomically, a group of neurons in the mouse primary visual cortex[58]. Two-photon calcium imaging was used to characterise functional properties, and large-scale electron microscopy of serial thin sections were employed to trace a portion of these neurons' local network). Other techniques can obtain whole brain structural gene expression information at the cellular level, as computationally reconstructed with histological (pixel size 0.95 μm^2) and MRI data (voxel size 12.3 μm^3) [1, 60, 2]. At the structural cellular level, other methods such as CLARITY enable estimations of the joint morphological statistics of many neurons in a tissue sample at the same time[62, 63]. For *in vitro* cellular approaches, scanning light microscopy (e.g., confocal microscopy) provides three-dimensional views of individual neurons but only down to ~1 μm resolution.

To date, several smaller-than-human-brain connectomes have been scanned, including the *C. elegans* connectome[64, 65, 66], the predatory nematode *Pristionchus pacificus* connectome[67], the connectomes of six interscutularis muscles[29], the partial structural and functional connectome of the mouse primary visual cortex (via electron microscope and two-photon microscopy, 800 TB data set, 5 nm x 5 nm x 50 nm spatial resolution, and the entire data set captures a tissue volume of 30×30×30

μm^3) [68], and the inner plexiform layer of the mammalian retina connectome (via automated transmission electron microscope imaging, 16.5 TB data set, ~2 nm resolution of a 0.25-mm-diameter tissue column spanning the inner nuclear, inner plexiform, and ganglion cell layers of the rabbit)[30].

Structural 3-D destructive reconstruction of a whole human brain with 20 μm resolution has been completed, preserving the first human whole-brain cytoarchitectural anatomy[3]. A planned future project is the creation of a ~1 μm spatial resolution brain model, intended to capture details of single cell morphology and to integrate gene expression data from the Allen Institute Brain Activity Map Project. There are also efforts underway to map the whole human brain at the synaptic level of resolution[70]. The remaining challenges necessary to scale these destructive processes into a whole human brain appear surmountable in the decades ahead.

Contemporary destructive approaches provide near-nanometric structural resolution, but many inherent problems remain. First, it is not clear if the different biomolecular machinery can be distinguished by the next generation of these techniques. Second, functional information is not captured by these techniques (although functional information might not always be necessary, in case atomic structural resolution is achieved). Third, destructive techniques are expected to face resistance for implementation in clinical practice, in part because the destruction is irreversible and in part because of the difficulty in proving the continuity of consciousness.

3. ACTION POTENTIAL MEASUREMENT REQUIREMENTS

The human connectome sets the underlying structure for the synaptic-processed (4.31 ± 0.86) x 10^{15} spikes/sec signal traffic processed in the whole human brain, constituting the most crucial and data-intensive information channel corresponding to (5.52 ± 1.13) x 10^{16} bits/sec [2]. Synapses, the structural sub-cellular components responsible for processing this data, play a crucial role in brain information processing[3], are involved in learning and memory (either long-term and short-term memory storage and deletion)[71, 72, 73, 74], participate in temporal processing of information[75], and are key elements for signal transduction and plasticity in the human brain[76, 77].

The key functional-information measurement task at synapses is monitoring action potentials, capturing even the fastest 400-800 Hz firing rates occurring at fast spiking neurons[4, 5] and the fastest voltage velocities at 20 mV/ms[6]. Inferable from the electrical data might be the action-potential-induced opening of ~20 Ca^{2+} channels per active zone, and consequent monitoring of ion fast release with a delay of 50–500 μs [78, 79]. Also potentially inferable might be the resultant Ca^{2+} transient (lasting 400–500 μsec)[79]. By measuring synaptic electrical activity, neuronanorobots can also monitor synaptic plasticity including synaptic based long-term potentiation, long-term depression, short-term plasticity, metaplasticity, homeostatic plasticity, and cross-talk.

Action potentials may encode information in spike timing pattern and in the spike waveform. While there is evidence that the action potential waveform encodes some type of information, its relevance is not clear. The rate of information transfer including action potentials waveforms may be significantly higher than the rate assuming only stereotyped spike train impulses[80]. In the interim, a conservative design criterion for action potential nanosensors would include the capacity to measure individual action potential waveforms.

For acquiring optimal spatial and temporal resolution the action potential nanosensors need to be positioned as close as possible to the action potential initiation site. In most cases, action potentials are initiated at the axon initial segments (AIS)[81], but in some cases action potentials are initiated at the axon hillock, and sometimes they are even initiated at the first node of Ranvier[82, 83]. For example, the site of action potential initiation in cortical layer 5 pyramidal neurons is ~35 μm from the axon hillock (in the AIS)[83]. In some other neuronal types, the action potential may be initiated at the first nodes of Ranvier[84, 85, 83] which, in layer 5 pyramidal neurons, is ~90 μm from the axon Hillock – the first myelin process is ~40 μm from soma and the length of the first myelin process is ~50 μm[83]. Since action potentials might be initiated in different cellular subcompartments, endoneurobots will be parked at the AIS (the most likely spot for action potential initiation) where they will monitor the large majority of action potentials. In neurons where some action potentials are initiated at the first nodes of Ranvier or the axon hillock, two synaptobots placed at the first node of Ranvier and at the axon hillock can ensure proper action potential waveform detection of all initiated action potentials.

Once in the right position, nanosensors will detect individual action potentials with proper waveform temporal resolution. Estimating the necessary waveform temporal resolution requires an overview of a neuron's firing frequency variability and theoretical maximum firing frequency. It is well-known that the "typical" ~20 μm human neuron discharges 5-100 sec^{-1}, moving from -60 mV potential to +30 mV potential in ~1 ms. However, the variability of action potential frequencies is large and depends largely on the electrophysiological class of the neuron[2]. There are three main electrophysiological classes of neurons in the human brain[86, 87]:

Regular Spiking neurons (which fire at low rates and adapt to continuous stimuli) respond to a "typical" depolarizing stimulus of 0.3 nA with initial frequencies of 100 Hz in the first 2 ms, then accommodate during the following 50 ms to steady frequencies of about 30 Hz (usually range 20-50 Hz)[4, 5]. Regular Spiking firing frequencies can rise to 200-300 Hz [5] with each spike lasting for ~1 ms [5].

Fast Spiking neurons (which sustain very high firing frequencies with little or no adaptation) respond to a depolarizing stimulus of 0.3 nA with a sustained high frequency of 250-350 Hz, though discharges can sometimes reach the 400-800 Hz range[4, 5]; duration is usually 0.4-0.6 ms.

Bursting neurons (which generate clusters of spikes either singly or repetitively) respond to a depolarizing stimulus of 0.3 nA with a repetitive burst discharge, with an intraburst frequency of 300 Hz (the first burst might reach 600 Hz) and an interburst frequency of 40 Hz[88]. Bursting neuron

high-frequency (300–600 Hz) spike bursts recur at fast rates (30-50 Hz) within a certain range of membrane potentials[89, 90, 4, 88]. Bursting neurons have two main subtypes: intrinsically bursting (IB) and fast-repetitive bursting (FRB)). During sustained depolarization, IB neurons fire a short burst of 3-5 action potentials at ~200 Hz which becomes repetitive usually at frequencies around 5-15 Hz[5]. During sustained depolarization, FRB neurons fire bursts containing 25 spikes at frequencies from 200-600 Hz, with short spikes of ~0.6 ms bursts repeating regularly at 20-80 Hz[5].

The maximum firing frequency reported in all human electrophysiological neuron types is 800 Hz, although other vertebrates employ somewhat higher maximum firing frequencies, e.g., 2000 Hz for chicken[91, 92, 93, 94]. For non-vertebrates, the maximum firing frequency for mechanosensory neurons in copepod antennules with single neurons firing was a maximum frequency of 5000 Hz and sustaining frequencies of 3000–4000 Hz for up to 4 ms[95]. Comprehensive electrophysiological studies may be necessary to guaranty that such high frequencies do not occur anywhere in human brains.

A detailed recording of human action potential waveforms might conceivably require a 0.05 ms temporal resolution (the fastest voltage velocities at 20 mV/ms would require 0.05 ms resolution for having mV resolution). However, a somewhat lower temporal resolution is expected to be necessary because each spike is estimated to carry 7-10 bits of information[2], motivating the choice 0.1 ms (i.e., 10,000 Hz) temporal resolution in the present work. This resolution should permit detailed monitoring of a very large majority of neuroelectrical waveforms and will ensure the detection of even the fastest action potentials.

4. CHOICE OF NANOSENSOR FOR ACTION POTENTIAL MONITORING

At least two basic nanosensor types could potentially be used on an intracellular basis to detect individual action potentials: concentration-based nanosensors (Section 4.1) and electrical field-based nanosensors (Section 4.2). The choice is largely driven by the need for a nanosensor that provides the required signal resolution necessary to characterise the action potential waveform. Thermal sensors, a third type, appear marginal because the thermal time constant across a distance $L_n \sim 20$ μm (the maximum diameter of human nerve axons) for neurons having thermal conductivity $K_t = 0.6$ W/m-K (~water at 310 K) and heat capacity $C_V = 4 \times 10^6$ J/m^3-K (brain tissue) is $\tau_{eq} = L_n^2 C_V / K_t \sim 3$ ms, much longer than the minimum ~0.1 ms temporal resolution that is probably required to sufficiently characterise fast spike waveforms.

4.1. Concentration-Based Nanosensors

One approach to monitor action potential waveforms is to use nanosensors that can directly measure the Na^+ and K^+ ion concentration changes intracellularly, near the axon membrane in the interior of the axon hillock during an electrical event. Typically, the resting ion concentrations in the cytosolic axoplasm are $[Na^+]_{in} = 18.0$ mM (1.1×10^7 ions/μm^3) and $[K^+]_{in} = 140.0$ mM (8.4×10^7 ions/μm^3), while extracellular concentrations are $[Na^+]_{out} = 144$ mM and $[K^+]_{out} = 4$ mM [96]. While an action potential event causes a $V_m \approx 100$

mV change in the neuron membrane potential as a result of entering Na^+ ions and exiting K^+ ions, the respective concentrations inside and outside of the axoplasm change relatively little when compared to the total number of Na^+ and K^+ ions present. This change in membrane potential is associated with a certain total number of charges that move across the plasma membrane per unit area, creating a charge differential across the membrane of $Q_{action} = C_m V_m / q_e \approx 6250$ ions/μm^2, taking membrane capacitance $C_m \sim 1$ $\mu F/cm^2$ for biological lipid bilayers[97] and $V_m \sim 100$ mV across the biological membrane, with each monovalent ion carrying one elementary charge $q_e = 1.6 \times 10^{-19}$ coul.

Considering the neuron soma (cell body) as a whole, and assuming a "typical" 10 μm diameter neuron with a total soma surface area of $A_{soma} \sim 314$ μm^2 and volume $V_{soma} \sim 524$ μm^3, the neuron cytoplasm contains $N_{Na+} = [Na^+]_{in} V_{soma} \sim 5.8 \times 10^9$ Na^+ ions and $N_{K+} = [K^+]_{in} V_{soma} \sim 4.4 \times 10^{10}$ K^+ ions. During an action potential, n_{Na+} ($=n_{K+}$) $\sim A_{soma} Q_{action} \sim 2 \times 10^6$ Na^+ ions enter the cell and an equal number of K^+ ions exit the cell. Such a small ion current represents an increase of only $\Delta C_{Na+} = n_{Na+} / N_{Na+} \approx 0.03\%$ in the sodium ion concentration of the entire neuron soma, and an increase of only $\Delta C_{K+} = n_{K+} / N_{K+} \approx 0.005\%$ for potassium ions during the rise time of the action potential. (Of course, overall Na^+ and K^+ concentrations can depart significantly from these values in axons having small cytoplasmic volumes when firing sustainedly at high frequencies.)

A more complete analysis would include the diffusion rates of ions and the number density of Na^+ and K^+ channels and pumps in order to account for the much slower pump rate per square micron by which the ions are returned to their original side of the membrane. Since the turnover rate of Na^+/K^+ pumps (~500 ions/sec) is so much slower than the Na^+/K^+ channels (~10^6-10^7 ions/sec), some increase in ion concentrations in the near-membrane volume might also be expected during fast spiking rates, consequently reducing the available concentration change for later action potentials. Ionic species can become highly hydrated when dissolved in water. For instance, a naked proton (H^+) is usually present as $H_5O_2^+$ or $H_7O_3^+$, or even as $H_9O_4^+$ in strong acid solutions[98], and some ions such as Li^+ and I are found in large solvent cages coordinated to as many as 46 water molecules[99, 100]. Another complicating factor is that little is known about the compartmentalization and dynamics of sodium and potassium fluxes in neuron cells with complex cytoarchitectures[101].

An ideal concentration sensor, limited only by diffusion constraints and drawing through a spherical boundary surface of radius R_s, provides a minimum detectable concentration differential of $\Delta c/c = (1.61 \Delta t D_0 c_{ion} R_s)^{-1/2}$, where Δt = measurement time, D_0 = aqueous diffusion coefficient of the hydrated ion at infinite dilution, and c_{ion} = ion concentration[102]. Requiring $\Delta t \leq 0.1$ ms to ensure minimally adequate action potential waveform resolution, then $R_{s/Na+} \geq 3.9$ μm to detect a $\Delta c/c = \Delta C_{Na+} = 0.03\%$ change in Na^+ ion concentration from the cytosolic baseline of $c_{ion} = 1.1 \times 10^7$ ions/μm^3 for Na^+, and $R_{s/K+} \geq 12.3$ μm to detect a $\Delta c/c = \Delta C_{K+} = 0.005\%$ change in K^+ ion concentration from the cytosolic baseline of $c_{ion} = 8.4 \times 10^7$ ions/μm^3 for K^+, taking $D_0 \sim 1.6 \times 10^{-9}$ m^2/sec for Na^+ and $D_0 \sim 2.4 \times 10^{-9}$ m^2/sec for K^+, in water at 310 K [103]. These values for R_s are already infeasibly

large but are only lower limits because the indicated $\Delta c/c$ occurs over a ~1 ms rise time, not over the shortest measurement interval $\Delta t \sim 0.1$ ms, hence the required $\Delta c/c$ detection threshold may be as much as tenfold lower. These considerations appear to rule out the use of chemical concentration sensors for real-time action potential monitoring inside living human neurons.

4.2. Electrical Field-Based Nanosensors

Another approach to monitoring action potential waveforms is to use nanosensors that can measure the change in local electric field strength during the action potential event. The electric field E (volts/m) surrounding a single monovalent ion is given by Coulomb's law as: $E = q_e / 4 \pi \varepsilon_0 \kappa_e r^2$, where $q_e = 1.60 \times 10^{-19}$ coul (one charge), $\varepsilon_0 = 8.85 \times 10^{-12}$ F/m (permittivity constant), κ_e = dielectric constant (relative permittivity) of the matter traversed by the electric field (e.g., taking $\kappa_e = 74.31$ for pure water at 310 K; κ_e decreases slightly with salinity[104]), and r = distance from the charge, in meters. In an aqueous medium such as the interior of an axon, the field at a distance of 10-100 nm from the singly-charged ion is 200,000-2,000 V/m.

Patch clamp is an existing laboratory technique that allows the study of single or multiple ion channels in neurons. The method combines scanning ion conductance microscopy, which is used to scan the exterior surface and identify the positions of ion channels on the neuron membrane, with patch-clamp recording through a single glass nanopipette probe[26]. The blunt-ended nanopipette, which has an inside diameter of 100-200 nm and can be positioned with nanometer precision, is first scanned over the neuron membrane area of ~0.03 μm^2, using current feedback to obtain a high-resolution topographic image. The tip is then sealed onto the membrane by applying suction to develop a tight high-resistance seal, guaranteeing that all ions fluxing the membrane patch flow into the pipette to be recorded by a chlorided silver electrode connected to a highly sensitive electronic amplifier. This method, also called nanopatch-clamp[105, 106, 107, 108], in principle allows the counting of each ion passing through a selected individual sodium or potassium ion channel. A single ion channel conducts between 1-10 million ions/sec, a current of 1-10 pA [109].

For nanorobots operating inside a neuron, permanently sealing a sensor around the cytosolic aperture of a large number of ion channels would be logistically challenging and would likely interfere with normal neuron function, e.g., ion transport and protein recycling. If we seek instead to measure ion current without sealed clamping of the sensor to the cell membrane, it is useful to examine the changes caused by the different types of noise in neurons that might affect sensor accuracy[110]. Sources of response variability in neurons and neural networks may include thermal noise, ionic conductance noise, ion pump noise, ion channel shot noise, synaptic release noise, synaptic bombardment, chaos, connectivity noise, and environmental stimuli[111, 112, 113, 114, 115, 116, 117].

After considering these potential sources of noise, the main conclusion is that thermal noise is the only source of noise relevant to evaluate if the cytoplasmic-resident nanosensors must be capable of distinguishing the entrance of each single

ion on the nearest ion channel without having a nanopatch-clamp sealed around the ion channel aperture.

The theoretical thermal noise limit for electric field detection using a "passive" cylindrical sensor of radius R = 25 nm, length L = 250 nm, and wall electrical thickness d_{wall} = 10 nm has been estimated [118] as: $E_{limit} = 2\sqrt{2}\ (k_B T\ d_{wall} / 4\ \pi\ \varepsilon_0\ \kappa_e)^{1/2}\ [1 / (R^{1/2}\ L^{3/2}\ (\nu\ t_{meas})^{1/2})] \sim 2000$ V/m, taking Boltzmann's constant k_B = 1.38 x 10^{-23} J/K, T = 310 K, electric field frequency ν = 10 KHz, measurement time t_{meas} = 0.1 ms, and relative permittivity $\kappa_e \sim$ 2000 for the wall material (cf., values approaching $\kappa_e \sim$ 100,000 at 310 K and ~KHz frequencies are reported for the perovskite-related oxide $CaCu_3Ti_4O_{12}$ [119]). A well-designed "passive" electric nanosensor of this size and configuration, when pressed near the axonal internal membrane surface, should readily detect the passage of one or a small number of ions and thus the variation in electric field caused by each action potential discharge, without resort to patch-clamping.

The density of Na^+ ion channels in the AIS of the axon is estimated as 100-200 μm^{-2} [81], so channels are spaced ~100 nm apart across the membrane surface. An R = 25 nm nanosensor placed 10 nm directly beneath an ion channel in the membrane would reliably detect the initial 200,000 V/m field from the entry of single Na^+ ions through the local channel, whereas Na^+ ions entering through the nearest adjacent channel 100 nm away and flowing around a second R = 25 nm nanosensor will be at closest 50 nm from the first nanosensor, generating a 8000 V/m field, just 4% of the local signal.

Exiting K^+ ions can also be detected if the potassium ion channel locations are known. Kv1 potassium channels [120] control axonal action potential waveform and synaptic efficacy, shaping the waveform in the AIS of layer 5 pyramidal neurons independent of the soma[121]. The first 50 μm of the AIS has a 10-fold increase in Kv1 channel density[121]. Considering the lifetime of a "typical" sodium or potassium ion channel, the Kv1.3 potassium channel has an estimated turnover rate (half-life) of 3.8 ± 1.4 hr, rising to ~6.3 hr in the presence of TrkB[122]. This is consistent with reported half-lives on the order of hours for ion channels on the cell membranes of cardiomyocytes[123], and suggests that our cytosolic-resident nanosensors may need to be repositioned and retargeted several times a day to maintain proper signal. A small array of sensors will also be required because target ion channel proteins will be rapidly drifting in and out of range of individual cytosolic nanosensors during long monitoring times – lateral diffusion time in cell membrane for transmembrane ion channel proteins is of order $t_D \sim X^2 / 2\ D_L \sim$ 0.1-1 sec between submembrane nanosensors located X = 40 nm apart, taking lateral diffusion coefficient $D_L \sim$ 0.001-0.01 μm^2/sec for Na+ ion channels at the axon hillock and neuritic terminal[124].

However, "passive" electrodes have a theoretical minimal size due to impedance because the sensing process in such detectors requires electrochemical ionic exchange. In "active" electrodes, such as the two-terminal transistors found in Field Effect Transistor (FET) based nanosensors, there is no similar exchange and the device/electrolyte interface has effectively "infinite" impedance. In such sensors, impedance is not relevant to recording

bandwidth or noise, allowing FETs to detect action potentials independently on the device/electrolyte interface and permitting nanosensor probe miniaturisation to smaller sizes[125]. Decreasing sensor size is beneficial because capacitance decreases and resistance terms are relatively improved or not limiting, so the RC time constant remains very small.

The smallest "active" FET-based nanosensor that has been built and tested has a probe of 40 nm diameter and 50 nm length, and has demonstrated good SNR[126].

5. PROPOSED FET-BASED NEURO-ELECTRIC NANOSENSOR

FET-based nanosensors can record electric potentials intracellularly in living neurons[127, 128] using kinked nanowire structures (Fig. 1), providing high signal-to-noise ratio (SNR) and high temporal resolution[125]. The voltage rise/fall time-frame ranged from 0.1 to 50 ms, with the FET nanosensors demonstrating capacity to detect 0.1 ms action potentials pulse rise/fall without detectable delay[129]. Thus, SWCNT or DWCNT FET-based nanosensors seem to be a promising technology for nanorobotic monitoring of action-potential based electrical information.

Fig 1. *(A) experimental 3-D free-standing, kinked nanowire FET bent probe; the yellow arrow and pink star mark the nanoscale FET. Scale bar, 5 μm (Reprinted with permission) [127, 131]. (B) Differential interference contrast microscopy images of an HL-1 cell and 60° kinked nanowire probe whose V-shaped apex is visible inside the cell (Reprinted with permission) [127]. (C) Experimentally-recorded intracellular action potential peak using FET sensors with kinked nano-wire gate, from cells cultured on polydimethylsiloxane substrate, with intracellular cytosolic resting potential indicated by the dashed line (Reprinted with permission)[129].*

However, common FET-based sensor components such as metal electrodes, if operated inside the neuron cell, would disrupt the normal functioning of the cell[125]. Existing design proposals reflect the present state of fabrication technologies and assume that nanosensor components must function extracellularly. *In vivo* intracellular action potential monitoring using FET-based nanosensors would also require miniaturisation of all the nanosensor components.

For our intracellular FET-based neuroelectric nanosensor (Fig. 2), a carbon nanotube ("Gate") connects the source ("*S*") and drain ("*D*") electrodes. The

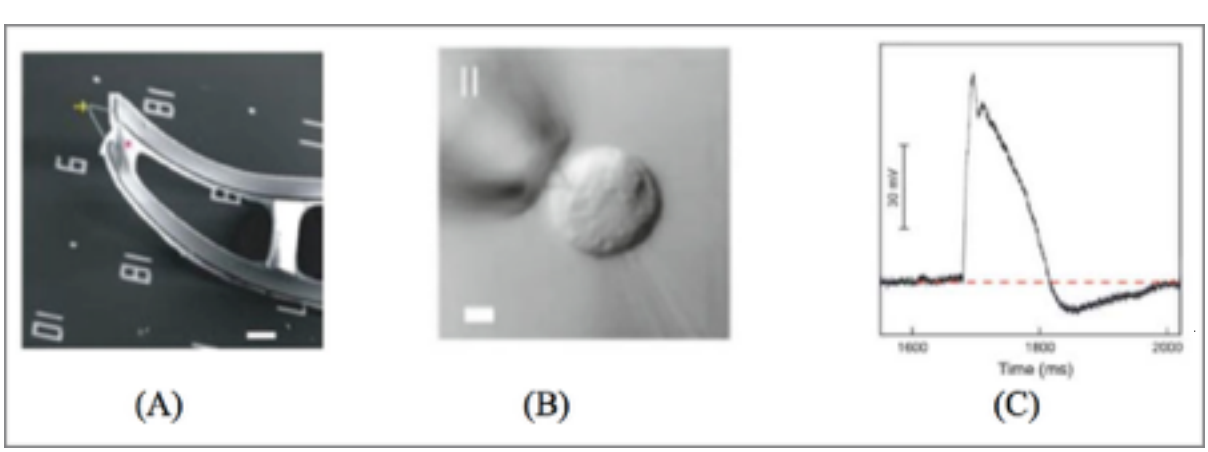

sensor also includes a voltmeter and ammeter, and receives power from a battery connected by nanowires. When immersed in the electrolytic environment of the neuron cytosol, only the nanotube gate is physically exposed to cytosolic fluid and the dependence of the conductance on gate voltage makes our nanosensor an electrically-based voltage nanosensor (Fig. 3).

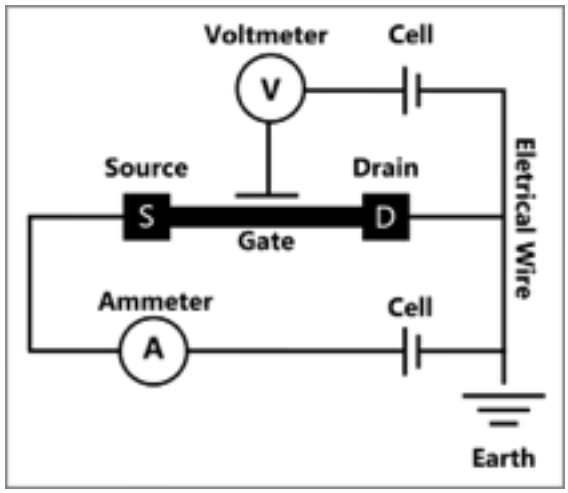

Fig 2. *Basic schematic of a FET-based neuroelectric nanosensor.*

Fig 3. *Vertical cross-section (side view, at left) and horizontal cross-section (top view, at right) of the FET-based neuroelectric nanosensor.*

The gate is composed of a single- or double-wall carbon nanotube. As the only structure interfacing the cytosol, the gate is a crucial component for sensor characteristics evaluation. CNT gates can route electrical signals at speeds up to 10 GHz when used as interconnects on semi-conducting devices. Double-wall carbon nanotube (DWCNT) based FETs might show metallic or semiconducting behavior depending on tube diameters, and are reported to be preferable to SWCNTs[130, 125]. FETs having a nanosensor interface with the neuron cytosol of 50 nm diameter provide an experimental bandwidth in the ~MHz range. For extracellular FET-based sensors, a nanosensor interface with the neuron cytosol as small as 3 nm has been modeled and provided a bandwidth ≥6 KHz, which would be good enough to record even the fastest 800 Hz action potential frequencies in humans[131, 125]. To avoid potential biocompatibility problems,

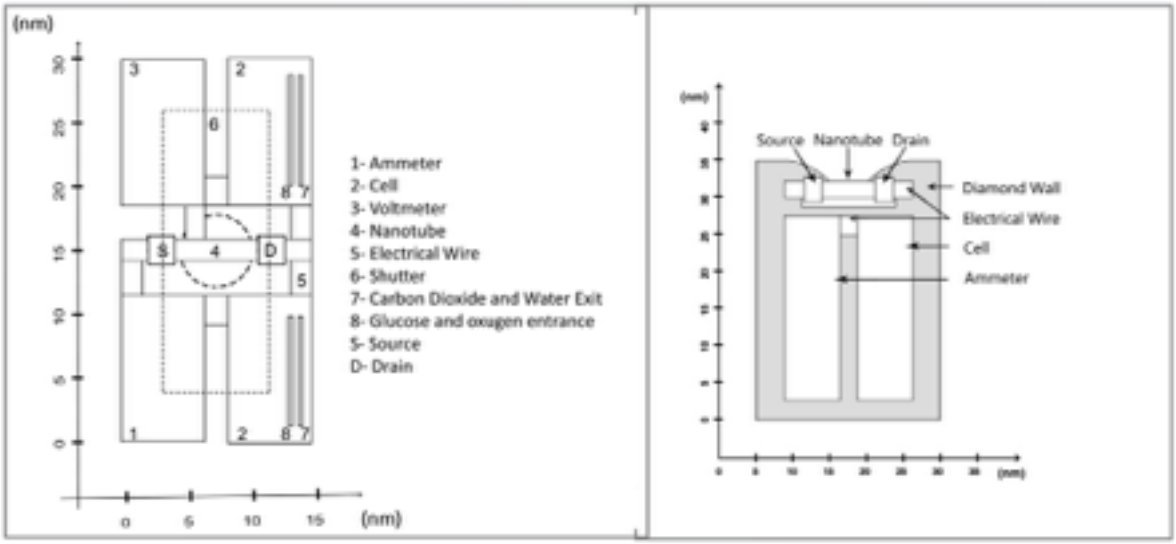

the CNT gate is likely to be in contact with an insulating substrate because semiconducting SWCNT-based FET nanosensors are sensitive to concentration, pH, internal water wetting, and ion type[132, 133].

Glass-coated hemispherical nanoelectrodes with dimensions as small as ~1 nm have been fabricated and exhibit reproducible and stable voltammograms without hysteresis, withstanding 6 hours of continuous use and 15 hours of iterative processes of heat and voltammetry[134, 135]. These types of nanoelectrodes offer several advantages: (1) mass-transport rate increase, allowing steady-state voltammetric responses to be readily achieved, (2) smaller RC constants, and (3) the ability to make measurements in solutions of high resistance because of the lower influence of solution resistance. The size and shape of the nanoelectrode is crucial because its electrochemical properties are often exceedingly sensitive to even small variations in its geometry.

Electrical measurement devices with tens of nanometer size are necessary to serve as ammeters and voltage detectors[125]. The smallest ammeters are expected to be electron ammeters that show the real-time dynamics of single electron tunneling[136] and provide high-sensitivity high-bandwidth single electron detection, measuring currents in the attoampere range (10^{-18} A) [137]. The charge detector employed might be a single-electron transistor or a double quantum dot to allow monitoring the direction of the flow of electrons[136, 137]. The double quantum dot can act as its own electrometer[136]. The ammeter might also be designed with the use of a small resistor and a sensitive current detector, such as a galvanometer, that converts electricity into a mechanical movement, possibly constructed within a 1000 nm^3 volume using the techniques of molecular manufacturing.

In the FET-based neuroelectric nanosensor, a voltmeter is placed in parallel with a circuit element to measure the voltage and must not appreciably change the circuit it is measuring. The nanosensor nano-voltmeter could employ traditional voltmeter concepts, using a current-limiting resistor followed by a small resistor, plus a galvanometer. Another option is to use voltage sensing inorganic nanoparticles (vsNPs) which are currently employed to self-insert into the cell membrane and optically record, non-invasively, action potentials at multiple sites and in a large field-of-view[138]. Alternatively, we might use an analog of the 30-nm "photonic voltmeter" which is one thousand times smaller than existing voltmeters and is claimed to enable complete 3-D electric field profiling throughout the entire volume of living cells[139].

The high conductivity of metallic nanotubes makes CNTs interesting building blocks for future advanced molecular electronic circuits[140]. SWCNTs are the most conductive carbon fibers known, with resistivity on the order of 10^{-4} ohm-cm at 27 °C and current density of ~10^{-7} A/cm^2, though in theory SWCNTs may be able to sustain stable current densities up to ~10^{-13} A/cm^2. In DWCNTs the difference between the radius of the inner tube and the outer tube is ~3.6 Å, independently of the DWCNT circumference, with the lattice structures of inner and outer tubes having no translational symmetry. Thus, the intertube transfer is negligibly small and has no effect on transport properties of DWCNT[141]. By managing the electronic

properties of CNTs (dependant on the orientation of the honeycomb lattice with respect to the tube axis, known as helicity), the neuroelectric nanosensor wires can be produced using DWCNTs[142]. Combining an internal CNT having metallic or semiconductor properties with an external nanotube having insulation properties gives a nanosensor wire that is a molecular analog of coaxial cable[142].

Some of the most important performance metrics on nanosensors are sensitivity, SNR, limit-of-detection, cross-sensitivity/ selectivity, signal rise/fall time (speed), repeatability, offset/sensitivity, drift, hysteresis, and lifetime/robustness[143]. These sensor characteristics must be futher evaluated experimentally in the context of the proposed neuroelectric nanosensor. For example, in extracellular recordings of cardiac myocytes an SNR of 2030 was measured for CNT based nanosensors (tenfold higher than competition)[145, 144]. An SNR of ~257 was determined for another CNT electrode during *in vitro* recording of neural signals in crayfish nerve cord[146]. A better SNR allows smaller signals to be detected, improving the sensor's limit of detection[147].

In the medical nanorobot implementation envisioned here, each endoneurobot will incorporate ~100 FET-based neuroelectric nanosensors in its outer hull (Fig. 4). Each nanosensor has ~3375 nm^3 volume (including power, housing and mechanical control, but not including control, communication and computational processing machinery). The endoneurobot nanosensors are organised in groups of ten nanosensors, distributed along the endoneurobot perimeter. While monitoring action potentials, at least one group of ten nanosensors should be near the axon membrane with nanosensor gates separated by ~40 nm.

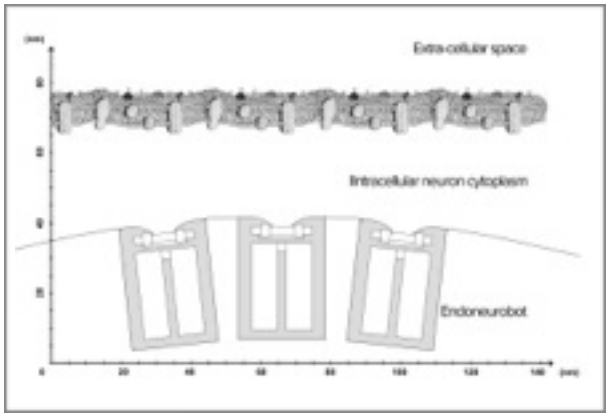

Fig 4. *A multitude of neuroelectric nanosensors, incorporated into the surface of a single endoneurobot, are positioned near the AIS membrane.*

6. SENSOR BIOCOMPATIBILITY

Our CNT-based FET nanosensor design must be carefully analysed to anticipate potential biocompatibility problems during intracellular neuron action potential monitoring. Neurons in general seem to accept carbon nanotubes – e.g., CNT-based substrates have proven to be biocompatible with neural cells and even stimulate neural cell growth, improving the cell's ability to extend processes and improving neuronal networks electrical performance[148, 149].

As the sensor gate is the only sensor component exposed to the neuron cytosol, one primary biocompatibility concern is the effect of carbon nanotubes on neural cells[150]. If a CNT gate is not physically disrupted, biocompatibility problems seem very unlikely because CNTs have demonstrated electrochemical and

biological stability[151], resistance to biofouling and mechanical compatibility with brain tissue[133]. The unlikely disruption, detachment and release into the neuron cytosol of a small number of CNT gates seems unlikely to cause problems on the cell. Only if CNTs are released in large quantities inside the neuron might cellular cytotoxic effects be induced. Depending upon shape and concentration, these effects could potentially include: (1) stronger than normal metabolic activity, (2) elevated lactate dehydrogenase, (3) generation of reactive oxygen species in a concentration- and time-dependent manner, indicating an oxidative stress mechanism, (4) activation of time-dependent caspase 3 showing evidence of apoptosis, (5) decrease of mitochondrial membrane potential, (6) increased level of lipid peroxide, and (7) decrease the activities of superoxide dismutase, glutathione peroxidase, catalase and the content of glutathione[148]. The effects on cell viability will vary in a concentration dependent manner (Fig. 5).

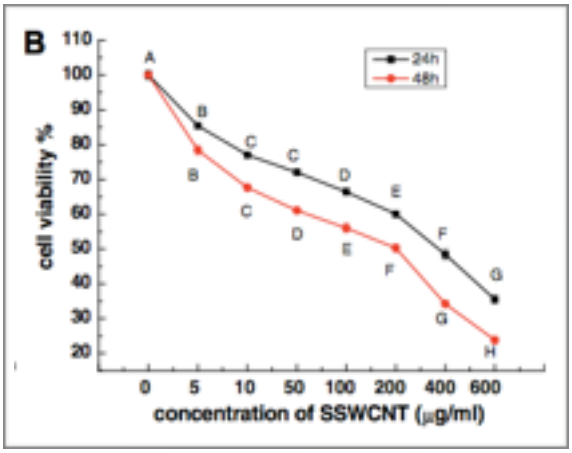

Fig 5. *Effect of short SWCNTs (SSWCNTs) on PC12 cell viability, when cells are treated with 500-2000 nm long SWCNTs for 24 and 48 hr at 37 °C (Reprinted with permission)[153].*

Short SWCNTs are defined as nanotubes with 1-2 nm diameter and 0.5-2 μm length, or more than 100 times longer than the proposed FET-based nanosensor gate. Consequently higher concentrations are expectably necessary to produce an equivalent effect on cell viability. A 10% reduction on cell viability corresponds to a 5 μg/ml concentration of short SWCNT. The release of all hundred 15-nm long FET-based nanosensor gates on one endoneurobot into the cytosol of a (20 μm)^3 volume neuron would amount to a ~0.001 μg/ml dose, causing a likely undetectable 0.002% reduction in cell viability.

Another biocompatibility problem might be hysteresis. The FET nanotube gate, lying on a SiO_2 surface, is very likely to exhibit hysteresis in its electrical characteristics due to charge trapping by water molecules around the nanotube, regardless of CNT hydrophobicity[152]. A protocol for closing the sensors and removing the water, perhaps using a shutter-like system or a set of molecular pumps, should reduce transistor hysteresis. Another solution is to create a virtually hysteresis-free transistor by passivating the nanotube with polymers that hydrogen bond with silanol groups on SiO_2 (e.g., with polymethyl methacrylate)[152]. The shutter-system is also useful for periodically cleaning the nanosensor surface to remove attached proteins.

The Young's modulus of SWCNTs depends on their size and chirality, but averages 1.09 TPa for a generic nanotube, hence CNTs are stiffer than steel and very

resistant to damage from physical forces, implying a long nanosensor lifetime and robustness. CNTs have strong in-plane graphitic carbon-carbon bonds which make them exceptionally strong and stiff against axial strains. Tenfold redundancy per group of sensors should preserve mission-long functionality. Protocols for removal and replacement of the endoneurobot should also be in place to handle unanticipated problems.

7. CONCLUSION

Comprehensive preservation of human brain information requires proper scanning of functional connectome data using appropriate nanosensors. Neuronanorobots (both endoneurobots and synaptobots) equipped with the proposed ~3375 nm^3 FET-based neuroelectric nanosensors might provide adequate temporal resolution for preserving action potential waveform information and could detect even the fastest human action potential firing rates of 800 Hz while presenting minimal biocompatibility problems. A set of such neuroelectric nanosensors installed on a sufficient number of well-placed endoneurobots and synaptobots will enable these robots to non-destructively and continuously monitor virtually all action potentials arising throughout a living human whole brain.

ACKNOWLEDGMENTS

The principal author (NRBM) thanks the "Fundação para a Ciência e Tecnologia" (FCT) for their financial support of this work (grant SFRH/BD/69660/2010).

REFERENCES

1. Azevedo, F.A., et al. (2009) Equal numbers of neuronal and nonneuronal cells make the human brain an isometrically scaled-up primate brain. J Comp Neurol. 513(5):532-41.
2. Martins, N.R.B., Erlhagen, W., Freitas, R.A. Jr. (2012) Non-destructive whole-brain monitoring using nanorobots: Neural electrical data rate requirements. Intl. J. Machine Consciousness 4(June 2012):109-140.
3. IBM (2008) IBM Seeks to Build the Computer of the Future Based on Insights from the Brain. IBM News Room, 20 Nov 2008. Website: https://www-03.ibm.com/press/us/en/pressrelease/26123.wss
4. Wilson, H. R. (1999) Simplifed Dynamics of Human and Mammalian Neocortical Neurons. Journal of Theoretical Biology. Volume 200, Issue 4, Pages 375-388.
5. Contreras, D. (2004) Electrophysiological classes of neocortical neurons.

Neural Networks Volume 17, Issues 5-6, Pages 633-646. June-July 2004.

6. Naundorf, B., et al. (2006) Unique features of action potential initiation in cortical neurons. Nature 440: 1060–1063.
7. Freitas, R.A. Jr. (1999) Nanomedicine, Volume I: Basic Capabilities. Landes Bioscience, Georgetown, TX.
8. Freitas, R.A. Jr. (1998) Exploratory Design in Medical Nanotechnology: A Mechanical Artificial Red Cell. Artif. Cells, Blood Subst., and Immobil. Biotech. 26:411-430.
9. Freitas, R.A. Jr. (2003) Nanomedicine, Volume IIA: Biocompatibility. Landes Bioscience, Georgetown, TX.
10. Morris, K. (2001) Macrodoctor, come meet the nanodoctors. Lancet 357(2001):778.
11. Astier, Y., et al. (2005). Protein components for nanodevices. Current Opinion in Chemical Biology 9(6), 576-584.
12. Patel, G. M., et al. (2006) Nanorobot: A versatile tool in nanomedicine. Journal of Drug Targeting 14(2), 63-67.
13. Park, H. H., et al. (2007) Rise of the nanomachine: The evolution of a revolution in medicine. Nanomedicine 2(4), 425-439.
14. Popov, A. M., et al. (2007) Biocompatibility and applications of carbon nanotubes in medical nanorobots. International Journal of Nanomedicine 2(3), 361-372.
15. Martel, S., et al. (2009) Flagellated magnetotactic bacteria as controlled MRI-trackable propulsion and steering systems for medical nanorobots operating in the human microvasculature. International Journal of Robotics Research 28(4), 571-582.
16. Mallouk, T. E., Sen, A. (2009) Powering nanorobots. Scientific American 300(5), 72-77.
17. Kostarelos, K. (2010) Nanorobots for medicine: How close are we?. Nanomedicine (Lond). 2010 Apr;5(3): 341-2.
18. Mavroides, D., Ferreira, A. (eds.) (2011) NanoRobotics: Current Ap-

proaches and Techniques (Springer, New York, 2011).

19. Freitas, R.A. Jr. (2006a) Chapter 13. Progress in Nanomedicine and Medical Nanorobotics, in Rieth M, Schommers W, eds., Handbook of Theoretical and Computational Nanotechnology**,** Volume 6 (Bioinformatics, Nanomedicine, and Drug Design), American Scientific Publishers, Stevenson Ranch, CA, pp. 619-672.
20. Freitas, R.A. Jr. (2010) Chapter 23. Comprehensive Nanorobotic Control of Human Morbidity and Aging. *in* Fahy, G.M., et al., (2010) The Future of Aging: Pathways to Human Life Extension, Springer, New York, pp. 685-805.
21. Freitas, R.A. Jr. (2000a) Clottocytes: artificial mechanical platelets. Institute for Molecular Manufacturing, Report No. 18, June 2000.
22. Freitas, R.A. Jr. (2000b) Nanodentistry. J. Amer. Dent. Assoc. 131(Nov): 1559-1566.
23. Freitas, R.A. Jr. (2005) Microbivores: Artificial Mechanical Phagocytes using Digest and Discharge Protocol. J. Evol. Technol. 14(Apr):1-52.
24. Freitas, R.A. Jr. (2006b) Pharmacytes: An Ideal Vehicle for Targeted Drug Delivery. J**.** Nanosci. Nanotechnol. 6(Sep/Oct):2769-2775.
25. Freitas, R.A. Jr. (2007) The Ideal Gene Delivery Vector: Chromallocytes, Cell Repair Nanorobots for Chromosome Replacement Therapy. J. Evol. Technol**.** 16:1-97.
26. Gorelik, J. (2002) Ion channels in small cells and subcellular structures can be studied with a smart patch-clamp system. Biophys J. 2002 Dec;83(6): 3296-303.
27. Freitas, R.A. Jr., Phoenix, C.J. (2002). Vasculoid: A personal nanomedical appliance to replace human blood. J. Evol. Technol. 11(April):1-139.
28. Sporns O., et al. (2005) The Human Connectome: A Structural Description of the Human Brain, PLoS Comput Biol 1(4).
29. Lu, J. Q., (2009) 3-D hyperintegration and packaging technologies for micro-

nano systems. Proc. IEEE, vol. 97, no. 1, pp. 18–30, Jan. 2009.

30. Anderson, J.R., et al. (2011) The Viking viewer for connectomics: scalable multi-user annotation and summarization of large volume data sets. J Microscopy: 241:13-28 (2011).
31. Kleinfeld, D., et al. (2011) Large-scale automated histology in the pursuit of connectomes. Journal of Neuroscience 31(45), 16,125-16,138.
32. Seung, H. S. (2011) Neuroscience: Towards functional connectomics. Nature 471, 170-172.
33. Seo, D., et al. (2013) Neural Dust: An Ultrasonic, Low Power Solution for Chronic Brain-Machine Interfaces. arXiv, 2013, arxiv.org/abs/1307.2196.
34. Hogg, T., Sretavan, D.W. (2005). Controlling tiny multi-scale robots for nerve repair. In Proc. of the 20th Natl. Conf. on Artificial Intelligence (AAAI2005), pages 1286–1291. AAAI Press, 2005.
35. Hogg, T., (2007) Coordinating Microscopic Robots in Viscous Fluids. Auton Agents Multi-Agent Syst 2007; 14: 271-305.
36. Freitas, R.A. Jr. (2009) Chapter 15. Computational Tasks in Medical Nanorobotics, in Eshaghian-Wilner MM, ed., Bio-inspired and Nano-scale Integrated Computing. John Wiley & Sons, NY, pp. 391-428.
37. Freitas, R.A. Jr., Merkle, R.C. (2006). Nanofactory Collaboration, 14 June 2006.
38. Freitas, R.A. Jr., Merkle, R.C. (2004) Kinematic Self-Replicating Machines**,** Landes Bioscience, Georgetown, TX.
39. Freitas, R.A. Jr. (2013) Chapter 6. Diamondoid Nanorobotics, *in* Mavroidis, C., Ferreira, A., eds., (2013) NanoRobotics: Current Approaches and Techniques, Springer, New York.
40. Kandel, E.R., et al. (2000) Principles of Neural Science (Fourth Edition). New York, McGraw Hill. 2000.
41. Johnson, G.A., et al. (2010) Waxholm Space: An image-based reference for coordinating mouse brain research.

NeuroImage, 2010; 53 (2): 365 DOI: 10.1016/j.neuroimage.2010.06.067.

42. Fiala, J.C., Harris, K.M. (2001) Extending unbiased stereology of brain ultrastructure to three-dimensional volumes. J Am Med Inform Assoc. 2001 Jan-Feb;8(1):1-16.
43. Wolters Kluwer Health: Lippincott Williams & Wilkins (2012, August 20). High-definition fiber tractography is major advance in brain imaging. ScienceDaily. Retrieved July 4, 2013, from http://www.sciencedaily.com /releases/ 2012/08/120820121050.htm.
44. Fernandez-Miranda, J.C., et al. (2012) High-definition fiber tractography of the human brain: neuroanatomical validation and neurosurgical applications. Neurosurgery. 2012 Aug;71(2):430-53. doi: 10.1227/NEU.0b013e3182592faa.
45. General Electric (2013) Phoenix Nanoatom S. Website: http://www.ge-mcs.com/en/radiography-x-ray/ct-computed-tomography/nanotom-s.html
46. Tkachuk, A, et al. (2007) X-ray computed tomography in Zernike phase contrast mode at 8 keV with 50-nm resolution using Cu rotation anode X-ray source. Zeitschrift für Kristallographie, vol. 222, issue 11, pp. 650-655.
47. Biswal, B.B., et al. (2010) Toward discovery science of human brain function. Proceedings of the National Academy of Sciences 107:10 4734-4740 (2010).
48. Nishimoto, S., et al. (2011) Reconstructing Visual Experiences from Brain Activity Evoked by Natural Movies. Current Biology, 21, 1641–1646.
49. Hayworth, K.J., et al. (2006) Automating the collection of ultrathin serial sections for large volume TEM reconstructions. Microscopy and Microanalysis 12 (Suppl 2):86-87.
50. Anderson, J. M., et al. (2009). Physiology and Function of the Tight Junction. Cold Spring Harbor Perspectives in Biology, 1(2), a002584.
51. Hayworth, K.J. (2012) Electron imaging technology for whole brain neural circuit mapping; International Journal of Machine Consciousness Vol. 4(01): 87-108.

52. Helmstaedter, M., et al. (2011) High-accuracy neurite reconstruction for high-throughput neuroanatomy. Nat Neurosci 14:1081-1088.
53. Livet, J., et al. (2007) Transgenic strategies for combinatorial expression of fluorescent proteins in the nervous system. Nature 450 (7166): 56–62.
54. Lichtman, J., et al. (June 2008) A technicolour approach to the connectome. Nature Reviews Neuroscience 9 (6): 417–422.
55. Zador, A.M., et al. (2012) Sequencing the Connectome. PLoS Biol 10(10): e1001411.
56. Withers, P.J., (2007) X-ray nanotomography, Materials today, Volume 10, Issue 12, December 2007, Pages 26–34.
57. Helmholtz Association (2010) New microscope reveals ultrastructure of cells. Public Release: 19 Nov 2010; http://www.eurekalert.org/pub_releases/2010-11/haog-nmr111910.php
58. Bock, D.D., et al. (2011). Network anatomy and in vivo physiology of visual cortical neurons. Nature. 2011;471:177–182.
59. Allen Brain Atlas - Website: ©2014 Allen Institute for Brain Science. Allen Human Brain Atlas [Internet]. Available from: http://human.brain-map.org/.
60. Hawrylycz, M.J., (2012) An anatomically comprehensive atlas of the adult human brain transcriptome. Nature 489, 391–399 (20 September 2012).
61. Allen Mouse Atlas - Website: ©2013 Allen Institute for Brain Science. Allen Developing Mouse Brain Atlas [Internet]. Available from: http://developing-mouse.brain-map.org.
62. Chung, K., Deisseroth, K. (2013) CLARITY for mapping the nervous system. Nature Methods 10(6), 508-513. June 2013.
63. Chung, K., et al. (2013) Structural and molecular interrogation of intact biological systems; Nature 497, 332–337. May 2013.
64. White, J.G., et al. (1986) The structure of the nervous system of the nematode

Caenorhabditis elegans. Phil Trans R Soc Lond B 314: 1–340.

65. Cheng, D., et al. (2006) Relative and Absolute Quantification of Postsynaptic Density Proteome Isolated from Rat Forebrain and Cerebellum. Molecular & Cellular Proteomics 5:1158-1170, 2006.
66. Varshney, L.R., et al. (2011) Structural Properties of the Caenorhabditis elegans Neuronal Network, PLoS Comput Biol. 2011 February; 7(2).
67. Bumbarger, D.J., et al. (2013). System-wide Rewiring Underlies Behavioral Differences in Predatory and Bacterial-Feeding Nematodes. Cell, Volume 152, Issue 1, 109-119, 17 January 2013.
68. Kaynig, V., et al. (2013) Large-Scale Automatic Reconstruction of Neuronal Processes from Electron Microscopy. Medical image analysis, 03/2013; 16(1).
69. Amunts, K., et al. (2013). BigBrain: An Ultrahigh-Resolution 3D Human Brain Model. Science 21 June 2013: Vol. 340 no. 6139 pp. 1472-1475.
70. OCP - Open Connectome Project (2014) Website: http://www.openconnectomeproject.org
71. Black, J.E., et al. (1990). Learning causes synaptogenesis, whereas motor activity causes angiogenesis, in cerebellar cortex of adult rats. Proc. Nati. Acad. Sci. USA, Vol. 87, pp. 5568-5572, July 1990.
72. Bliss, T.V., et al. (1993) Collingridge A synaptic model of memory: long-term potentiation in the hippocampus. Nature 361, 31 - 39 (07 January 1993).
73. Kandel, E.R. (2001) The molecular biology of memory storage: A dialogue between gene and synapses. Science 294 (5544): 1030–1038.
74. Liu, X., et al. (2012) Optogenetic stimulation of a hippocampal engram activates fear memory recall. Nature, 484, 381–385.
75. Fuhrmann, G., et al. (2002) Coding of Temporal Information by Activity-Dependent Synapses The Journal of Neurophysiology Vol. 87 No. 1 January 2002, pp. 140-148.

76. Rollenhagen, A., Lübke, J.H.R. (2006) The morphology of excitatory central synapses: from structure to function, Cell Tissue Res (2006) 326:221–237.

77. Rollenhagen, A., et al. (2007) Structural determinants of transmission at large hippocampal mossy fiber synapses. J. Neurosci. 2007 Sep 26;27(39): 10434-44.

78. Sabatini, B.L., Regehr, W.G. (1996) Timing of neurotransmission at fast synapses in the mammalian brain. Nature 384:170–72. 1996.

79. Südhof, T.C. (2004) The synaptic vesicle cycle, annual Review of Neuroscience Vol. 27: 509-547.

80. Polavieja, G. G., et al. (2005) Stimulus History Reliably Shapes Action Potential Waveforms of Cortical Neurons; J Neurosci. 2005 Jun 8;25(23):5657-65.

81. Kole, M.H., et al. (2008) Action potential generation requires a high sodium channel density in the axon initial segment, Nat Neurosci 11 (2008), pp. 178–186.

82. Sanford L., (1968) The axon hillock and the initial segment; The Journal of Cell Biology, Vol 38, 193-201, 1968.

83. Palmer, L.M., Stuart, G.J. (2006) Site of Action Potential Initiation in Layer 5 Pyramidal Neurons. The Journal of Neuroscience, February 8, 2006, 26(6): 1854-1863.

84. Colbert, C.M., et al. (1996) Axonal Action-Potential Initiation and Na+ Channel Densities in the Soma and Axon Initial Segment of Subicular Pyramidal Neurons. J Neurosci. 1996 Nov 1;16(21):6676-86.

85. Clark, B.A., et al. (2005) The site of action potential initiation in cerebellar purkinje neurone. Nature Neuroscience 8, 137 - 139.

86. Connors, B.W., Gutnick, M.J. (1990). Intrinsic firing patterns of diverse neocortical neurons. Trends in Neuroscience 13(3), 99-104.

87. Tateno, T., et al. (2004) Threshold Firing Frequency–Current Relationships of Neurons in Rat Somatosensory Cortex: Type 1 and Type 2 Dynamics;

JN Physiol October 1, 2004 vol. 92 no. 4 2283-2294.

88. Steriade, M. (2004) Neocortical Cell Classes Are Flexible Entities; Nature Reviews Neuroscience 5, 121-134.
89. Steriade, M., et al. (1998) Dynamic properties of corticothalamic neurons and local cortical interneurons generating fast rhythmic (30-40 Hz) spike burst. Journal of Neurophysiology 79(1), 483-490.
90. Wang, X. J. (1999) Fast burst firing and short-term synaptic plasticity: A model of neocortical chattering neurons. Neuroscience. 1999 Mar;89(2): 347-62.
91. Rubel E.W., Parks, T.N. (1975) Organization and development of brain stem auditory nuclei of the chicken: tonotopic organization of n. magnocellularis and n. laminaris. J Comp Neurol. 1975, 164:411–433.
92. Berry, M.J., et al. (1998) Refractoriness and neural precision. J Neurosci, 18 (6), 2200-2211.
93. VanRullen, R., Thorpe, S.J. (2001); Rate Coding vs Temporal Order Coding: What the Retinal Ganglion Cells tell the Visual Cortex. Neural Comput. 2001 Jun;13(6):1255-83.
94. Kuznetsova, M.S., et al. (2008) Adaptation of Firing Rate and Spike Timing Precision in the Avian Cochlear Nucleus; J Neurosci. 2008 November 12; 28(46): 11906–11915.
95. Fields, D.M., Weissburg, M.J., (2004) Rapid firing rates from mechanosensory neurons in copepod antennules; J Comp Physiol A (2004) 190: 877–882. DOI 10.1007/s00359-004-0543-2.
96. Cressman, J.R. Jr, et al. (2009) The influence of sodium and potassium dynamics on excitability, seizures, and the stability of persistent states: I. Single neuron dynamics. J Comput Neurosci. 2009 Apr;26(2):159-70.
97. Fettiplace, R. et al. (1971) The thickness, composition and structure of some lipid bilayers and natural membranes. The Journal of Membrane Biology. 1971, Volume 5, Issue 3, pp 277-296

98. Clever, H.L. (1963) The Hydrated Hydronium Ion. J. Chem. Ed. 40. December 1963):637-641.

99. Israelachvili, J.N. (1992) Intermolecular and Surface Forces, Second Edition, Academic Press, NY, 1992.

100. Lehr, L., et al. (1999) Electron Solvation in Finite Systems: Femtosecond Dynamics of Iodide-(Water)n Anion Clusters. Science 284(23 April 1999): 635-638.

101. Dubach, J. et al. (2008) Abstract 1879: Novel Intracellular Sodium Nanosensors to Study Sodium Dynamics in Cardiomyocytes. Circulation 2008;118:S-399.

102. Berg, H.C., et al. (1977). Physics of Chemoreception. Biophysical Journal 20(1977):193-219.

103. Li, Y., Gregory, S. (1974) Diffusion of ions in sea water and in deep-sea sediments. Geochimica et Cosmochimica Acta 38(1974):703-714.

104. Gadani, D.H., et al. (2012) Effect of salinity on the dielectric properties of water. Indian J. Pure Appl. Phys. 50(June 2012):405-410.

105. NanoMedLabs (2010) Nano Patch-Clamp (NPC): Development of a High-Throughput System Based On Planar Patch-Clamp. 15 July 2010. Website: http://www.nanomed.unige.it/Projects/NPC.htm

106. Electronic BioSciences (2013) High performance single ion channel recordings at a low cost. Website: http://www.electronicbio.com.

107. Novak, P., et al. (2013) Nanoscale-Targeted Patch-Clamp Recordings of Functional Presynaptic Ion Channels. Neuron 79, 1067-1077.

108. Electronic BioSciences (2014) Website: www.electronicbio.com/Nanopatch/

109. Veitinger, S. (2011) The Patch-Clamp Technique:An Introduction. Website: http://www.leica-microsystems.com/science-lab/the-patch-clamp-technique/

110. DeFelice, L.J. (1981) Introduction to Membrane Noise. Plenum Press, New York.

111. Lauger, P. (1984) Current noise generated by electrogenic ion pumps. Eur Biophys J 11(2): 117-128.

112. Hô, N., Destexhe, A. (2000) Synaptic background activity enhances the responsiveness of neocortical pyramidal neurons. J. Neurophysiol. 84, 1488.

113. Li, C., et al. (2001) Chaos in a three-neuron hysteresis hopfield-type neural networks. Physics Letters A, 285, 368-372.

114. Gerstner, W., Kistler, W.M. (2002) Spiking Neuron Models: Single Neurons, Populations, Plasticity, Cambridge University Press (August 2002).

115. Brunetti, R., et al. (2007). Shot noise in single open ion channels: A computational approach based on atomistic simulations. Journal of Computational Electronics 6(1): 391-394.

116. Serletis, D., et al. (2011) Complexity in neuronal noise depends on network interconnectivity. Ann Biomed Eng 39(6): 1768-1778.

117. Birn, R.M., (2012) The role of physiological noise in resting-state functional connectivity. Neuroimage, 62(2), 864-870. doi: 10.1016/j.neuroimage.2012.01.016.

118. Weaver, J.C., Astumian, R.D. (1990) The Response of Living Cells to Very Weak Electric Fields: The Thermal Noise Limit. Science 247:459-462.

119. Homes, C. C., et al. (2001) Optical Response of High-Dielectric-Constant Perovskite-Related Oxide. Science 293(27 July 2001):673-676.

120. Gutman, G.A., et al. (2005) Nomenclature and Molecular Relationships of Voltage-Gated Potassium Channels. Pharmacol Rev 2005 57: 473-508.

121. Kole, M.H., et al. (2007) Axon Initial Segment Kv1 Channels Control Axonal Action Potential Waveform and Synaptic Efficacy; Neuron. 2007 Aug 16;55(4):633-47.

122. Colley, B.S. et al. (2007) TRKB increases Kv1.3 ion channel half-life and surface expression; Neuroscience. 2007 January 19; 144(2): 531–546.

123. Smyth, J.W., Shaw, R.M., (2010), Forward trafficking of ion channels:

What the clinician needs to know. Heart Rhythm. 2010 Aug;7(8):1135-40.

124. Angelides K.J. et al. (1988) Distribution and lateral mobility of voltage-dependent sodium channels in neurons. J. Cell Biol. 106, 1911-25.

125. De Vittorio, M. et al. (eds.) (2014), Nanotechnology and Neuroscience: Nano-electronic, 13 Photonic and Mechanical Neuronal Interfacing, ISBN 978-1-4899-8038-0. Springer 2014.

126. Cohen-Karni, T., et al. (2012) Synthetically Encoded Ultrashort-Channel Nanowire Transistors for Fast, Pointlike Cellular Signal Detection, Nano Lett. 2012;12;2639−2644.

127. Tian, B., et al. (2010) Three-dimensional, flexible nanoscale field-effect transistors as localized bioprobes. Science 13 August 2010: Vol. 329 no. 5993 pp. 830-834.

128. Chen, K., et al. (2011). Silicon nanowire field-effect transistor-based biosensors for biomedical diagnosis and cellular recording investigation. Nano Today, Volume 6, Issue 2, April 2011, Pages 131–154.

129. Duan, X., et al. (2013); Nanoelectronics Meets Biology: From New Nanoscale Devices for Live-Cell Recording to 3D Innervated Tissues; Chem. Asian J. 2013, 8, 2304 – 2314.

130. Shimada, T., et al. (2004) Double-wall carbon nanotube field-effect transistors: Ambipolar transport characteristics, Appl. Phys. Lett. 84, 2412.

131. Duan, X., et al. (2011) Intracellular recordings of action potentials by an extracellular nanoscale field-effect transistor. Nat Nanotechnol 7: 174-179.

132. Cao, D. et al. (2012) Electronic sensitivity of a single-walled carbon nanotube to internal electrolyte composition. Nanotechnology, 2012 Mar 2;23(8):085203.

133. Yoon, I., et al. (2013) Intracellular neural recording with pure carbon nanotube probes, PLoS One. 2013 Jun 19;8(6).

134. Aoki, K., et al. (2010) Fabrication of glass-coated electrodes with nano and

micrometer size by means of dissolution with HF. Electrochimica Acta, Volume 55, Issue 24, 1 October 2010, Pages 7328–7333.

135. Cox, J.T., et al. (2012); Nanoelectrodes: Recent Advances and New Directions. Annu. Rev. Anal. Chem. 2012. 5:253–72.

136. Lambert, N. J., et al. (2014); A charge parity ammeter, 2014 American Chemical Society, Nano Lett. 2014, 14, 1148−1152.

137. Fujisawa, T. (2006) Bidirectional Counting of Single Electrons. Science, June 2006. Vol. 312 no. 5780 pp. 1634-1636.

138. Park, K., et al. (2012) Single Molecule Quantum Confined Stark Effect Measurements of Semiconductor Nanoparticles at Room Temperature. ACS Nano, 2012, 6, 10013–10023.

139. Tyner, K. M., et al. (2007). "Nano-sized Voltmeter" Enables Cellular-Wide Electric Field Mapping. Biophysical Journal, 93(4), 1163–1174.

140. Dergan, A. (2010) Electronic and transport properties of carbon nanotubes, University of Ljubljana, Faculty of Mathematics and Physics, 2010.

141. Uryu, S. (2004); Electronic states and quantum transport in double-wall carbon nanotubes, Physical Review B 69, 075402.

142. Bacsa, R.R. (2003) Narrow diameter double-wall carbon nanotubes: synthesis, electron microscopy and inelastic light scattering. New Journal of Physics 5:131.1–131.9;

143. Roman, C., et al. (2010) Single-Walled Carbon Nanotube Sensor Concepts; Springer Handbook of Nanotechnology, 2010, pp 403-425.

144. Nick, C. et al. (2012) Three-Dimensional Carbon Nanotube Electrodes for Extracellular Recording of Cardiac Myocytes. Biointerphases. 2012 Dec; 7(1-4):58.

145. Liu, S., Guo, X. (2012) Carbon nanomaterials field-effect-transistor-based biosensors. NPG Asia Materials. NPG Asia Materials (2012) 4, e23.

146. Lin, C.M., (2009) Flexible carbon nanotubes electrode for neural recording. Biosens Bioelectron. 2009 May 15;24(9):2791-7.

147. Mehrabani, S., et al. (2014) Hybrid Integrated Label-Free Chemical and Biological Sensors, Sensors 2014, 14, 5890-5928.

148. Zhang, Y. et al. (2010) Cytotoxicity Effects of Graphene and Single-Wall Carbon Nanotubes in Neural Phaeochromocytoma-Derived PC12 Cells. ACS Nano, 2010, 4 (6), pp 3181–3186.

149. Bosi,, S., et al., (2013) Carbon nanotubes: a promise for nerve tissue engineering?. Nanotechnol Rev 2013. 2(1): 47–57.

150. Silva, G.A. (2009) Shorting neurons with nanotubes. Nature Nanotechnology 4, 82-83.

151. Voge, C.M., Stegemann, J.P. (2011) Carbon nanotubes in neural interfacing applications. J Neural Eng 8.

152. Kim, W., et al. (2003) Hysteresis Caused by Water Molecules in Carbon Nanotube Field-Effect Transistors, Nano Letters 3(2):193-198.

153. Wang, J., et al. (2011) Cytotoxicity of single-walled carbon nanotubes on PC12 cells, Toxicology in Vitro 25. 242–250.